

Influence of built-in charge on photogeneration and recombination processes in InAs/GaAs quantum dot solar cells

S. Kondratenko^{a}, A. Yakovliev^a, S. Iliash^a, Y. Mazur^{b*}, M. Ware^b, Phu Lam^c, Mingchu Tang^c,
Jiang Wu^c, Huiyun Liu^c and G. Salamo^b*

^aDepartment of Physics, Taras Shevchenko National University of Kyiv,

64 Volodymyrs'ka St., Kyiv 01601, Ukraine

^bInstitute for Nanoscience and Engineering, University of Arkansas,

Fayetteville, Arkansas 72701, United States of America

^cDepartment of Electronic and Electrical Engineering, University College London,

Torrington Place, London WC1E 7JE, United Kingdom

**Corresponding author*

ABSTRACT: Selective doping of quantum dots is often used to improve efficiency of intermediate band solar cells (IBSC) due to IR harvesting and built-in-dot charge. To investigate the effects of the built-in-dot charge on recombination processes and device performance

InAs/GaAs quantum dot IBSCs with direct Si doping in the quantum dots are fabricated, and the I–V characteristics and transients of the open circuit voltage and short circuit current are measured. The decay times of both the open circuit voltage and the short circuit current increase as the concentration of n-type doping increases in the quantum dots. The observed increase in the charge carrier lifetime is attributed to suppressed recombination of electron-hole pairs through the states of quantum dots and shrinking the depletion layer. This is supported by measurements of both photovoltage and photoluminescence spectra.

I. INTRODUCTION

Among various technologies, tandem solar cells and intermediate band solar cells (IBSC) with low-dimensional objects are two of the most important designs toward increasing the solar power conversion efficiency over the classic Shockley-Queisser limit [1,2]. In IBSCs nanostructures, such as quantum dots (QDs) or quantum wires (QWRs) [3-9], can provide an extra optical transition due to the introduction of localized states (or intermediate bands) within the band gap of the host semiconductor material [2-14]. According to theoretical calculations, the maximum efficiency of an IBSC is 63.2%, exceeding the theoretical efficiency limit of 40.7% for solar cells based on a single semiconductor [15].

The concept of a quantum dot solar cell has been developed as a method of enhancing the photoelectric conversion efficiency [6]. Incorporation of quantum dots (QDs) into the space-charge layer of a contact or barrier layer [16] as well as into the intrinsic layer of *p-i-n* diodes are both promising for expansion of the spectral response to the IR range and increase of the short-circuit current without loss in the open-circuit voltage. However, despite the low concentration

of defects and dislocations in InAs QDs and their surrounding barrier material, the solar cell efficiency of devices with InAs QDs is commonly lower than a comparable GaAs-reference *p-i-n* diode [17]. For example, in comparison with a GaAs-reference *p-i-n* diode an increase of the external quantum efficiency of a *p-i-n* InAs/GaAs QD solar cell (QDSC) was observed in the near IR range below the bandgap of GaAs [18]. Unfortunately, inclusion of the QD layers in the intrinsic layer of the *p-i-n* diodes leads to an increase of the dark current and a decrease of the quantum efficiency resulting from an increase of carrier concentration and recombination rate. This is caused by the additional electron-hole recombination centers created by the InAs QDs in the *i*-GaAs [19]. Ultimately, this results in a slight decrease of the open circuit voltage. As a result, the losses due to QDs often negate the expected growth of photocurrent due to harvesting of the infrared photon energy and the improvement in conversion efficiency of the quantum dot solar cell does not exceed a few percent [12,20].

Among the various efforts to increase carrier lifetime and the associated short-circuit current in QD based SCs, *n*-type doping of the conventional InAs QDs or the GaAs spacer layers has demonstrated promising results [2,21,22]. Direct Si doping in InAs QDs, as was demonstrated earlier [22], leads to an improved open circuit voltage as large as 105 mV. This could be explained in terms of the reduced thermal coupling of QD states from the wetting layer (WL) and conductivity band in the GaAs QDSCs assisted by Si doping. One of the main reasons is that the negative charge which gets captured in the dots due to the doping prevents the capture of mobile electrons by the QDs and decreases Shockley-Read-Hall recombination in the space charge region. To further understand the recombination process, we investigate the effect of QDs on recombination and photogeneration processes using photovoltage and photocurrent transient

techniques as well as photoluminescence and photovoltage spectroscopy of *p-i-n* InAs/GaAs solar cells by applying Si dopants to the QDs.

II. EXPERIMENTAL DETAILS

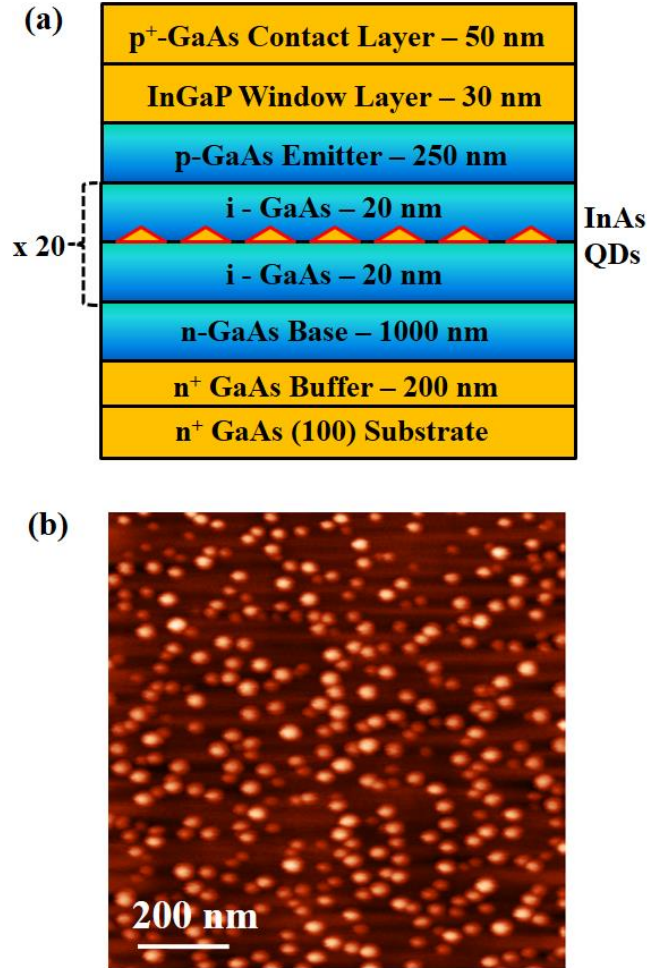


Figure 1. Growth diagram of InAs/GaAs QDSC (a) and AFM image of InAs QDs (b).

All the InAs/GaAs QDSC structures were grown by solid-source molecular beam epitaxy (MBE) on n^+ -GaAs(100) substrates. Figure 1a shows a schematic of the *p-i-n* diode, which has been described in detail in Ref.22. The intrinsic region of the *p-i-n* diode consisted of a superlattice of InAs QD layers separated by 20 nm GaAs spacers, repeated 20 times. The InAs QDs were formed through Stranski–Krastanov relaxation of 2.35 MLs of InAs deposited at a

substrate temperature of 470°C. During the QD growth, direct Si-doping is applied in order to supply 0, 6, 12, 18, and 24 electrons per QD. The doping density is calibrated using a QD average height of 3 nm, base average diameter 35 nm, and sheet density of $3 \times 10^{10} \text{ cm}^{-2}$ measured from atomic force microscope of the uncapped InAs QDs (Fig. 1b).

Post-MBE growth, the QDSCs were cleaned using acetone for 10 mins in an ultrasonic bath, the process was then repeated with isopropanol. To remove surface oxidation, the SC was immersed for 20 s in a 1:1 solution of concentrated hydrochloric acid and deionized water before rinsing in deionized water and dried with nitrogen. A gold–zinc alloy was thermally evaporated to form a grid-pattern p-type electrode with the use of a shadow mask. The thermally evaporated n-type electrode coated the back surface and consisted of following layers: nickel / gold–germanium / nickel / gold with thicknesses of: 5 nm / 150 nm / 50 nm / 200 nm, respectively. No anti-reflection coating was deposited in the fabrication of the SCs. The surface area was 0.7 cm^2 for the studied QDSCs.

Photoluminescence (PL) measurements were performed using the 532 nm line of a frequency doubled Nd:YAG laser for excitation. The PL signal from the sample was dispersed by a monochromator and detected by a liquid nitrogen cooled OMA V: InAs photodiode detector array.

The I - V curves were measured using a Picotest 3510A semiconductor analyzer. The spectral dependencies of the photoconductivity and the open circuit voltage, V_{OC} , were measured at excitation energies ranging from 1.1 to 2.0 eV using the illumination of a 250 W halogen lamp. The corresponding photocurrent or open circuit voltage was registered by lock-in amplification technique using a modulation frequency of 80 Hz. Spectral dependences were normalized to the constant number of exciting quanta using a nonselective pyroelectric detector.

The open circuit voltage and photocurrent temporal dependencies were recorded on a Siglent 70-MHz-bandwidth digital oscilloscope with pre-amplifier. Photocurrent transients were measured by applying a constant bias voltage to the cell using a voltage source. The SCs were excited using an optical pulse generated by a laser diode with emission at 650 nm and a pulse width of $\sim 60 \mu\text{s}$ with rise and decay times of $\sim 10 \text{ ns}$. The pulse intensity was set to create a $< 50 \text{ mV}$ shift in the barrier height of the $p-i-n$ diodes, thus the resulting transient measurements were performed at nearly constant bias conditions.

III. RESULTS AND DISCUSSION

Figure 2 shows the dark current-voltage ($I-V$) curves of InAs/GaAs SCs with different doping levels measured at room temperature. As seen, the current in the reverse bias is an order of magnitude lower than in forward bias.

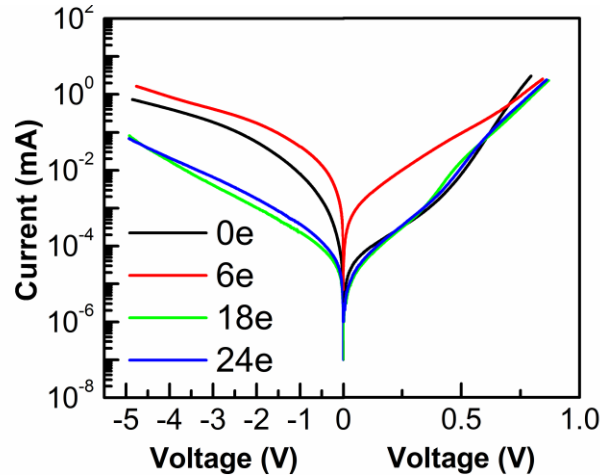


Figure 2. Dark $I-V$ curves measured on the InAs/GaAs solar cells doped with Si at 290 K.

The shape of curves was analyzed within the framework of the standard diode equation. Usually, the dark $I-V$ dependencies can be described by the diode model if the diffusion current and the recombination current are both present in a single diode. Here the current density, J , is given by:

$$J(V) = J_0 \left(\exp \left(\frac{e(V - IR_s)}{nkT} \right) - 1 \right) + \frac{V - IR_s}{R_{SH}}, \quad (1)$$

where J_0 is the diode reverse saturation current, k is the Boltzmann's constant, T is the absolute temperature, R_s and R_{SH} are the series and shunt resistance, respectively. The diode ideality factor is a characteristic of the generation-recombination (G-R) processes which dominate in the $p-i-n$ diodes. These are mainly considered as being active only in the space-charge region. It is commonly accepted that $n=1$ when the diffusion current is dominate and $n=2$ when the recombination current is dominate. For $p-i-n$ diodes with QDs in the intrinsic layer, G-R processes via QD states increases the ideality factor up to 3 or more[23].

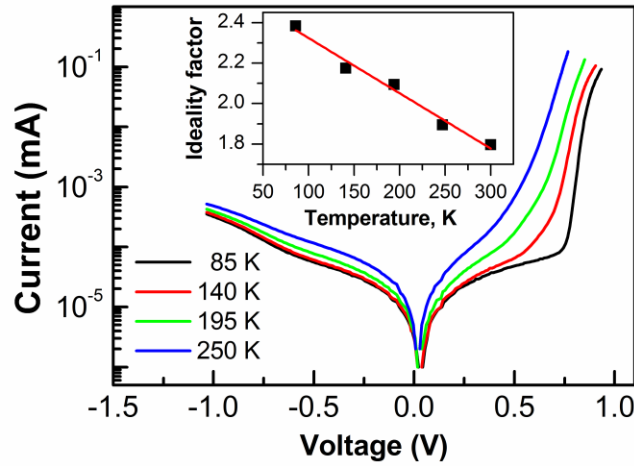


Figure 3. Dark I-V curves measured for the undoped reference QDSC samples at different temperatures. The inset shows the temperature dependence of the ideality factor.

At high voltage, $V > kT/e = 25$ mV, the forward bias branch of the $I-V$ curves is defined by the exponential term of Eq. 1 from which the ideality factor, n , may be determined. For the doped QD solar cells, the ideality factor shows weak temperature dependence, whereas it decreases linearly with temperature from $n = 2.4$ at 85 K to $n = 1.8$ at 290 K (see Fig. 3, inset) for the undoped sample due to increasing the recombination current via QDs. The ideality factor

is found to change non-monotonically with doping level with the 6 electrons per dot QDSC sample exhibiting the highest value of $n=3.4$ at 290 K. For this doping level and temperature, some portion of the QD states are not occupied by electrons, while practically all Si impurities in the QDs are ionized thermally. In such a case, besides the QD states, the impurities are additional recombination centres for electron-hole pairs in the space-charge region leading to the increase of n to 3.4 for 6e sample as compare with $n = 1.8$ for the undoped SC at 290 K. These large ($n>2$) values of the ideality factor for undoped and 6e samples are due to strong recombination current via states of InAs QDs and Si impurity levels (Shockley-Read-Hall process) in the space charge region of the *i*-GaAs, which can be much greater than the diffusion and drift currents for a low injection level[24]. With further increase in doping concentration, for the samples with 18 or 24 electrons per dot, the ideality factor is smaller and varies in the range of 2.0-2.2 at 290 K. This observation is a clear indication that heavy *n*-type doping decrease the probability of recombination via the QDs and the Si impurities. Filling the QD ground state suppresses electron flow from the *n*-GaAs to the space-charge layer of the *i*-GaAs due to Coulomb repulsion[25], which leads to decrease in the probability of electrons recombining with holes via QD levels and a reduction of the ideality factor.

The sample doped with 6e per dot, with the highest value of n , also exhibited the highest reverse saturation current. The variation of reverse saturation current with doping can be understood qualitatively as follows. Thermal ionization of shallow Si impurities causes an increase in the electron concentration in the QDs and in the space-charge region of the *i*-GaAs. Therefore, the reverse current will increase suddenly with the introduction of a low *n*-type doping level. At the same time, this doping suppresses the generation of electron-hole pairs directly in the QDs due to increased filling of the QDs by electrons. When the conduction band

states in the QDs are already filled, the interband transitions become forbidden and the generation rate of electron-hole pairs in the QDs is reduced sharply. As a consequence, the concentration of carriers released from the QDs to the space-charge region of the *p-i-n* diode becomes limited. As a result of these opposite trends, the reverse current initially increases with doping, reaches the maximum, and decrease due to filling of the QDs by electrons. Confirmation of this strong effect due to the *n*-type doping in the 18e and 24e samples on interband transitions due to filling of the QD ground states by electrons was obtained from photovoltage spectroscopy measurements.

Figure 3 presents *I-V* curves of the undoped sample, i.e. zero electrons per QD, measured at different temperatures. Both the forward and the reverse current increase with temperature. The current density at low reverse bias of a *p-i-n* diode depends on an effective thermal emission of electrons from the states in the conduction band of the QDs and/or the two-dimensional wetting layer. Since the quantization in the InAs QDs is much stronger in the growth direction, the electron emission rate can be considered using a two-dimensional electron concentration for the both the QDs and the WL states. Taking this into consideration, we can model the density of the electron emission current from the 2D localized states as [26]:

$$J_e = e_T \cdot n_{2D} \text{ ,} \quad (2)$$

where e_T is the thermal emission rate from the QDs and/or WL localized states and n_{2D} is the two-dimensional electron concentration. As a result, the temperature dependence of the emission current density in reverse bias can be described by the equation [27,28]:

$$J_e(T) \sim T^{1/2} \exp\left(-\frac{\mathcal{E}_a}{kT}\right) \text{ ,} \quad (3)$$

where $\varepsilon_a^{QD} = E_c - E_{QD}$ is the activation energy from the QD level E_{QD} with respect to the edge of the conduction band of the GaAs surroundings. Note that an equation similar to Eq.3 with $\varepsilon_a^{WL} = E_c - E_{WL}$ can be written for contribution of thermal emission of electrons from the WL states, E_{WL} . The inset to Figure 5 shows the conductivity band profile for one of QD's layer, where the activation energies, ε_a^{QD} and ε_a^{WL} , are marked with arrows.

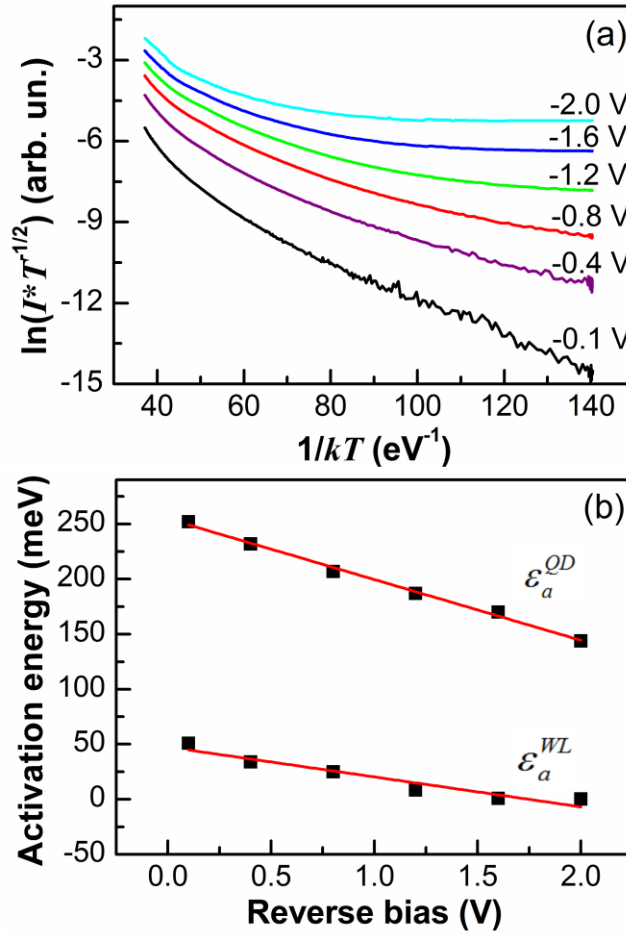


Figure 4. (a) Temperature dependencies of the current from undoped QDSC samples at different reverse bias. (b) Activation energies ε_a^{QD} and ε_a^{WL} for different reverse bias voltages applied to the sample.

The activation energies were obtained from the slope of linear part of the Arrhenius plot of the current temperature dependence $\ln(I \cdot T^{-0.5})$ vs. $1/kT$ as has been performed in Fig. 4a. Alternatively, the same energies were obtained when the all curves $I(T) \cdot T^{-0.5}$ were fitted with two-exponent function $C_1 \exp\left(-\frac{\varepsilon_a^{QD}}{kT}\right) + C_2 \exp\left(-\frac{\varepsilon_a^{WL}}{kT}\right)$, where C_1 and C_2 are constant. For reverse biases the complex temperature dependence of the dark current exhibited two activation energies of 51 and 250 meV at 0.1 V. The value of 250 meV corresponds to electron emission from the ground level of the QDs to the GaAs conduction band edge. The activation energy of 51 meV corresponds to thermal emission from the conduction band states of the WL to delocalized states of the GaAs. Both of these activation energies are found to decrease as the reverse bias is increased as is shown in Fig. 4b. This is explained by Poole-Frenkel emission from the potential well [29].

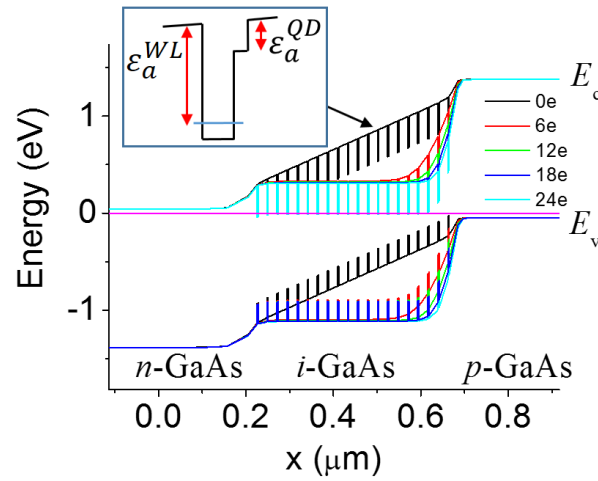


Figure 5. Simulated band structure of the QDSCs with different levels of Si doping. The inset shows the conductivity band profile for one of QD's layer, where the activation energies are marked with arrows.

In order to gain a clearer picture of the transport and optical properties of the system, energy band diagrams of the QD, *p-i-n* diode structure were calculated using Nextnano software[30] (Figure 5). In the undoped structure, 0e, the intrinsic region is characterized by a nearly constant electric field of 22.4·kV/cm, whereas the doped samples exhibit non-homogenous built-in fields due to ionized impurities alone. Additionally, though, strain fields surrounding the individual QDs have a strong impact on electronic properties [31], transport, and recombination of charge carriers [32]. To understand this, the three-dimensional strain was simulated in and around the QDs using a uniform half ellipsoid sitting on a two dimensional wetting layer as a model. We takes into account that formed QDs in Stranski–Krastanov mode are $\text{In}_x\text{GaAs}_{1-x}\text{As}$ alloy due interdiffusion of Ga and In between the QD and the surrounding GaAs matrix during. The In content of 0.38 provides the best agreement with the position of the PL band, while the QD average size was taken from AFM data. Figure 6a is a resulting two-dimensional cross-section of the $\text{In}_{0.32}\text{Ga}_{0.68}\text{As}$ QD and wetting layer showing the local deformation in the growth direction, ε_{zz} . Here we see that the deformation increases inside the QD until it reaches a maximum value of $\sim 2\%$. At the same time, we find ε_{zz} varies considerably in the plane perpendicular to the growth direction above and below the dot up to several tens of nanometers away. Similar strain maps around QDs were observed experimentally in Ref.32 by analyzing HRTEM images of InAs/GaAs QD heterostructures. The earlier observations show [32] that strain-induced shifts of the conduction band minimum and the valence band maximum in the GaAs layer causes bandgap variations of ~ 100 meV resulting in electric field values of $\sim 10^4$ V/cm in the vicinity of the QDs. In general, the local strain-induced fields slow down the recombination rate due spatial separation of the electron-hole pairs. At the same time, the ionized donors able to create the strong electric fields around the QDs. In order to compare these effects

we simulated energy band diagram for the undoped and the 24e, doped QDs taking into account strain map.

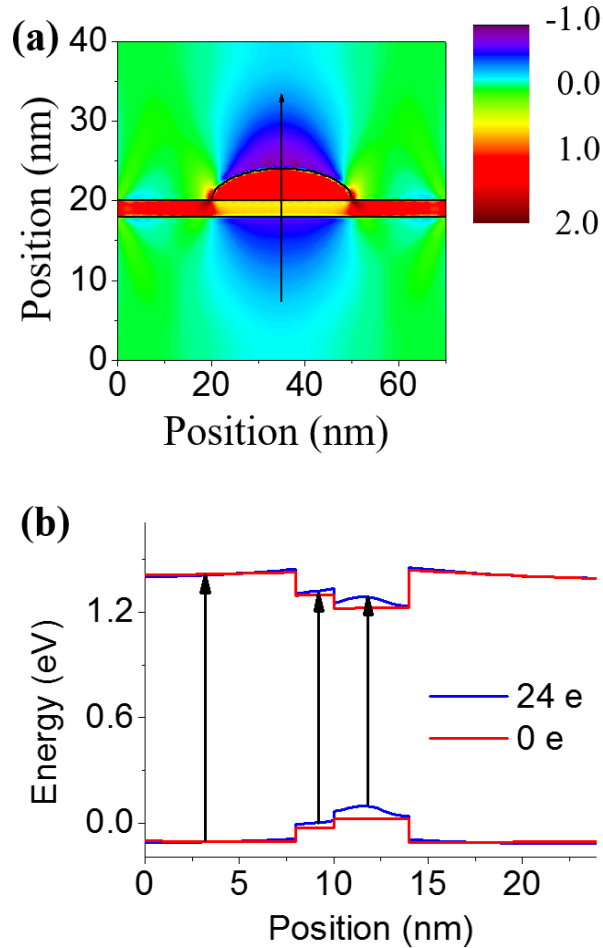


Figure 6. Simulated strain map (a) and energy band diagram for $\text{In}_{0.32}\text{Ga}_{0.68}\text{As}$ QDs in a GaAs matrix.

Figure 6b shows the energy band diagram for the undoped and the 24e, doped $\text{In}_{0.32}\text{Ga}_{0.68}\text{As}$ QDs, which was simulated by solving the three-dimensional Schrödinger equation taking into account the strain fields. We can see that electric field created by ionized donors inside QD was an order of magnitude higher than strain-induced fields. The presence of the undoped QDs creates electric fields up to 5.5 kV/cm due to the strain fields, locally, but has essentially no effect on the space charge region of $p-i-n$ diode. On the contrary, doping of the InAs QDs by Si

changes the potential profile dramatically. The intrinsic layer of the doped QDSCs consists of two regions with different electric fields. One region is characterized by large band bending towards the *p*-GaAs layer with much higher electric fields than the undoped QDSC. The other region exhibits a nearly flat band with a weak modulation of the electrostatic potential in and around the QDs created by ionized Si impurities (see Fig.6). This resulting strong electric field prevents capture of electrons and promotes trapping of holes by the QDs having strong impact on recombination and QDSC performance.

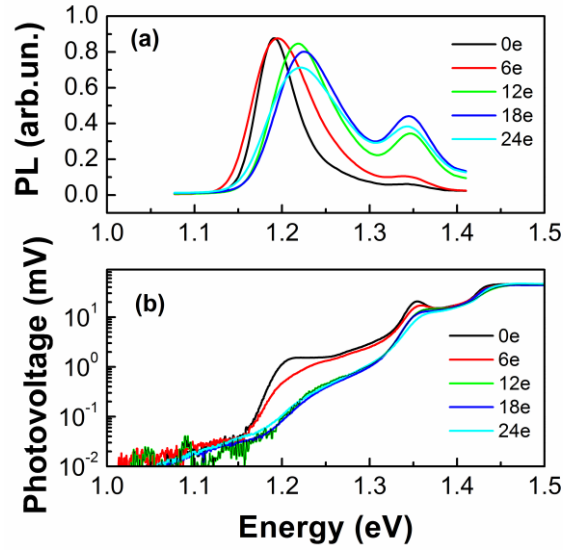


Figure 7. Photoluminescence (a) and photovoltage (b) spectra measured for the quantum dot solar cell samples with different doping levels in the QDs at 290 K.

Photovoltage and photoluminescence spectroscopy reveal several electronic transitions in our samples. Moreover, the shape of PL and PC spectra depends on doping level. The PL spectra of the solar cells measured at 290 K using 28 mW of 532 nm excitation from a Nd:YAG laser are shown in the figure 7a. The low energy band is associated with transitions between the quantum confined states of the InAs QDs, while the luminescence at $h\nu > 1.33$ eV was caused by transitions in the WL [22]. Figure 7b shows the photovoltage spectra of the QD solar cells with

different levels of doping. Band-to-band absorption in the GaAs is observed above 1.43 eV, absorption in the wetting layer is seen between 1.33 and 1.43 eV, and interband transitions in the InAs QDs correspond to the signal below 1.33 eV.

In order to give contribution to the photovoltage signal, electron-hole pairs, photoexcited in the QDs, must escape from potential well of the dots by thermal emission, Poole-Frenkel effect [33,34], phonon assisted tunnelling [35] or direct tunnelling [36], and be separated by electric field of the *p-i-n* diode. As seen in Figure 7b, doping reduces the long-wavelength (below bandgap of GaAs) photovoltage monotonically. At the same time, the greatest changes were observed for the components at $h\nu > 1.33$ eV, related to interband transition in the doped QDs. The main reason is that *n*-doping decreases the probability for photogeneration of electron-hole pairs in the InAs QDs due to increased filling by electrons of the ground states known as Burstein-Moss effect in the heavily doped semiconductors [37].

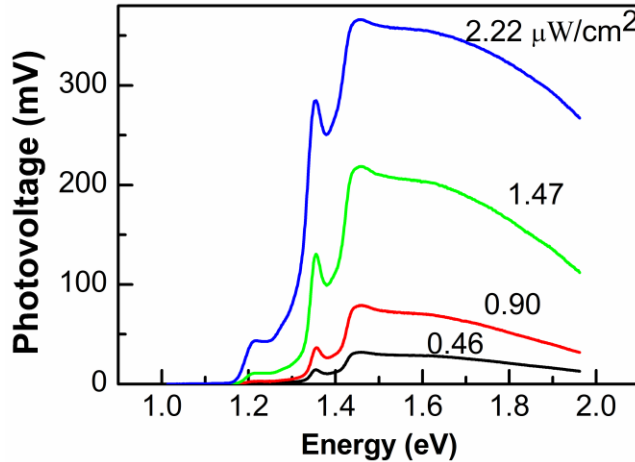


Figure 8. Photovoltage spectra measured at 290K for the undoped quantum dot solar cell at different illumination intensities.

The electrons in the *n*-doped QDSCs populate mainly the states of the QDs, which leads to the appearance of built-in fields in their surroundings [38]. The impact of such fields on the G-R

processes, carrier release from the QDs, and harvesting of IR energy is expected to be essential. To better understand the role of this built-in charge in the photogeneration of electron-hole pairs in the InAs QDs and subsequent contribution to the PV signal, we have measured the photovoltage spectra for the undoped InAs/GaAs quantum dot solar cell at different illumination intensities (Fig.8). Nonlinear changes in the PV spectral intensity curves were observed where the relative contribution to the PV signal of the QDs as compared to the GaAs matrix, above 1.43 eV, increases with intensity. Specifically, at low intensities $< 0.46 \mu\text{W}/\text{cm}^2$ the photovoltage due to the electron-hole pairs generated in the QDs near 1.21 eV is only about 3.3% of that due to the electron-hole pairs generated in the GaAs near 1.45 eV, while for high intensity, $2.22 \mu\text{W}/\text{cm}^2$, the photovoltage of the QDs reaches about 12 % of the PV signal in the GaAs.

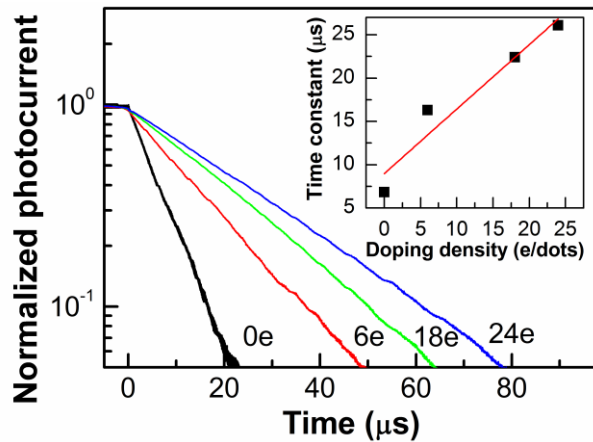


Figure 9. The decay of the photocurrent transients for the QDSCs with 0e, 6e, 18e, and 24e per QD after illumination from a 20 μs , 650 nm LED pulse. The transients were taken at a temperature of $T = 290\text{K}$ with the applied voltages held at zero using a load resistor, R_L , of 430 Ω . The inset shows the fitted time constants for all samples.

A critical question that needs to be addressed is the difference between optical pumping and the effect of doping on the photovoltage spectra and dot population. Since the activation energy of the holes from the QDs is much less than the activation energy of the electrons, band-to-band

excitation leads to accumulation of electrons in the QDs and creation of a depletion region around them. The nanoscale potential barriers around the QD/GaAs interfaces substantially suppress electron capture into QDs from the GaAs matrix, and enhance the photoresponse [39]. This effect is known for InAs/GaAs low-dimensional heterostructures as artificial doping, where the IR response is increased by resonant optical pumping due to an enhanced intraband transition rate from the localized states of the QDs to the conduction band states of the matrix [40]. Thereby, when studying the photovoltage signal induced by band-to-band transitions in the InAs QDs, we should take into account that accumulation of negative charges facilitates electron emission from the QDs and restricts their re-capture leading to non-linear increasing of QDs contribution to the PV spectrum with intensity. Note that the appearance of excess carriers both in localized states of the QDs and the GaAs matrix, then spatial redistribution of electron-hole pairs leads to a change in the potential profile around the QDs and contact potential difference of the *p-i-n* junction, enhancing nonlinear changes in the PV spectral shape. The described non-linearity as well as enlarged response of QDs in the narrow (1.16-1.33 eV) spectral range will be also observed under AM1.5G illumination. Therefore, we expected only the insignificant increase of the quantum efficiency with intensity due to improved IR harvesting. However, our observations give reason to conclude that an indirect effect of optical pumping on recombination via QDs, WL and GaAs states may be more important and requires further investigations.

To give further insight on features of the generation-recombination processes in the doped QDSCs, we investigate photovoltage and photocurrent transients. Fig.9 shows the photocurrent decay transients of the QDSCs after illumination with a 20 μ s pulse from a 650 nm LED. The transients were taken at a temperature of $T = 290$ K with zero applied bias voltage and a load resistance, R_L of 430 Ω . Photocurrent decays were found to be exponential with decay time

constants, τ , which scale linearly with the concentration of Si in the QDs (see inset to Fig.9). By varying the external load resistance, a linear dependency of τ was observed for all studied SCs. This indicates that the decay transients can be well described by a single RC discharging process with a capacitance of $C = \tau / R_L$, which can be extracted from the slope of the straight line (see Figure 10a). The cells capacitances are found to growth linearly with the concentration of Si in the QDs from $C = 11.89$ nF (17.00 nF/cm²) for the uncharged reference SC to $C = 47.74$ nF for the 24e sample. The observed increase of the junction capacitance could be explained by shrinking the depletion layer with doping due to the presence of the ionized donors in the intrinsic layer (see Fig.5b).

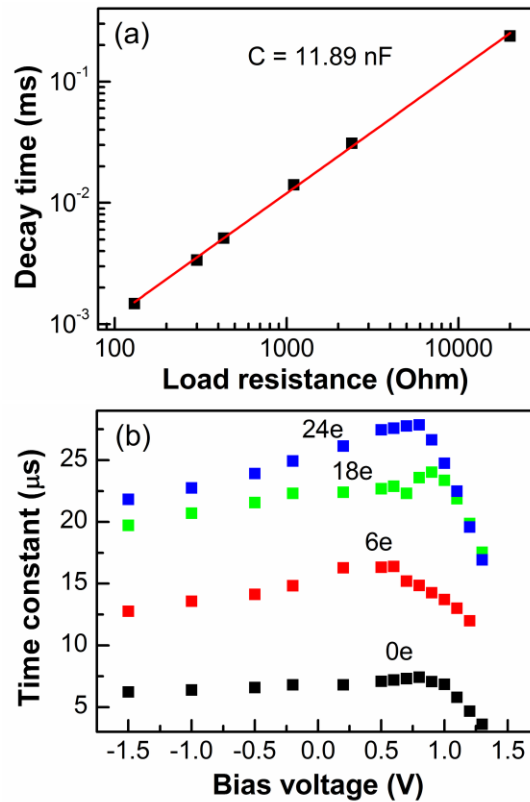


Figure 10. (a) Decay time constant vs the external load resistance for the undoped solar cell at 290 K. (b) The dependence of the photocurrent decay time constant on the bias voltage measured with a load resistor, R_L , of 430Ω .

Photocurrent transients were obtained throughout the bias range from -1.6 V to $+1.2$ V such that the decay time constants as functions of bias voltage could be analysed. The results of this for all samples are given in figure 10b. This shows directly that the origin of this capacitance is related to the properties of the quasi-neutral region of the *p-i-n* diodes. For reverse biased voltages and small forward biased voltages the junction capacitance is dominant. As the forward bias voltage is further increased, the minority carrier distribution in the quasi-neutral region increases exponentially and the junction capacitance decreases suddenly. When the forward bias voltage exceeds the barrier height, i.e., $V > V_b$, the decay time decreases drastically with voltage reaching a minimum value determined by the internal recombination processes of the device. The point in the $\tau(V)$ curve where the time constant suddenly decreases represents the *p-i-n* diode turn-on voltage, which is the device barrier for forward bias conduction. These were found to be $V_b = 0.79 \pm 0.10$ V and $V_b = 0.81 \pm 0.10$ V for undoped and 24e samples, respectively. This determination of the forward barrier agrees well with the V_{OC} values ranging from 0.777 V to 0.890 V for QDSCs under AM1.5G conditions [22].

Figure 11 shows the photovoltage transients of all samples, measured using a 20 μ s, 650 nm LED pulse with the sample at 290 K. We observe by comparing Figure 11a with 11b that the PV rise time is about 1 order of magnitude faster than the decay time for all studied cells. Here we also see that the PV signal reaches a higher value for the undoped QDSC and decreases as the doping level increases. This is due to the, still, relatively slow rise time of the QDSC samples with insufficient time to reach their saturation current within the 20 μ s light pulse.

At the same time the PV decay curves plotted in Figure 11b can be well described by a single exponent for each of the QD solar cells. In comparison with the photocurrent decay, the PV signal exhibited much slower transients. The undoped cell demonstrated the fastest time constant

with $\tau = 0.62$ ms, while increasing the doping results in longer time constants finally demonstrating a time of $\tau = 2.34$ ms for the cell with 24e per dot.

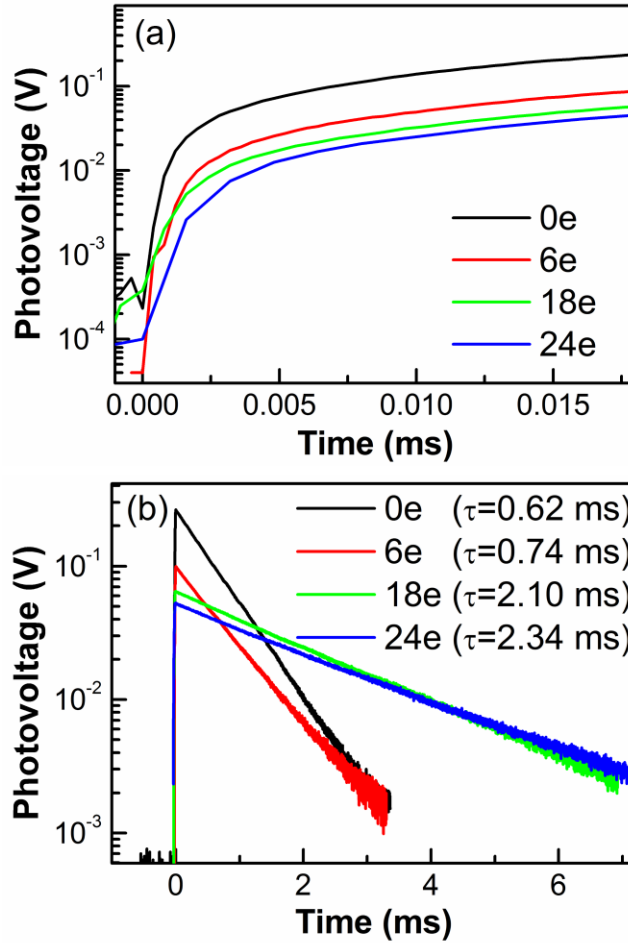


Figure 11. Transient photovoltage rise (a) and decays (b) of the QDSCs at 290 K after illumination from a 20 μ s, 650 nm LED pulse.

Figures 12a and 12b show the transient photovoltage rise and decay, respectively, of the undoped InAs/GaAs quantum dot solar cell after illumination from a 650 nm LED pulse using photoexcitation intensities ranging from 3 to 11.4 μ W/cm² at 290 K. Again, a *p-i-n* junction barrier height can be found in the saturation value of the open-circuit voltage, V_{OC} , at 0.66 ± 0.01 V. This can be best seen with the maximum excitation intensity of 11.4 μ W/cm² after ~ 0.01 ms

and further supports the value determined from the photocurrent decay, $V_b = 0.7 \pm 0.1$ V. The saturated value of the open-circuit voltage, probing with 650 nm illumination, is found to be lower than $V_{OC} = 0.777$ V observed earlier under AM1.5G illumination [22] due to surface recombination. Excitation of the QDSCs with a 650 nm light pulse leads to appearance of electron-hole pairs in the p -GaAs emitters at an absorption length of ~ 330 nm predominantly [25,41]. Some of them recombine via surface states of other kinds of centres in the intrinsic region. The rest are separated by the built-in electric field of the p - i - n diode resulting in the appearance of excess electrons near the n -GaAs, whereas the holes are shifted towards the p -GaAs contributing to V_{OC} .

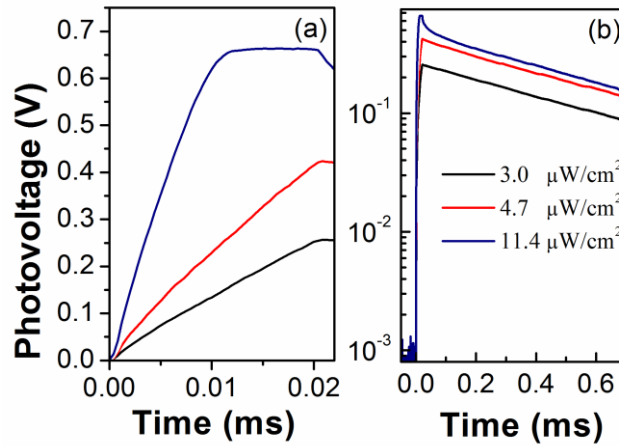


Figure 12. Transient photovoltage rises (a) and decays (b) of the undoped QDSC at 290 K after illumination from a 20 μ s, 650 nm LED pulse with different intensities.

It should be also noted, for excitation with $3.0 \mu\text{W}/\text{cm}^2$ pulses the transient photovoltage rise was found to be linear, however at higher intensities it demonstrated a non-linear, non-exponential behaviour (Fig.12). This indicates that the rise and decay of the PV transients can't be described by a single RC (dis)charging process.

In this case, the time constant is determined by the time of carrier transport through the depletion layer of the *p-i-n* junction, where electron-hole recombination including the QD states takes place. As a result, the recombination rate is determined by the rate of hole supply to the space-charge region, which due to the relative mobility in GaAs is much smaller than the rate of electron supply [42]. As described above, the built-in electric field of the *p-i-n* diode increases with doping, whereas the depletion region becomes narrower (Fig.5). Where in most of the QD layers are in the flat-band region. Without a drift component of the current flow, hole supply extends the open-circuit voltage decay. Moreover, the observed variation of the potential profile in and around the QDs as well as the presence of traps slows the recombination rate via the quantum states of InAs increasing the decay constant of the PV signal with doping.

All of our observation, i.e. the *I-V* measurements, photovoltage and photocurrent transients at different biases and excitation intensities, simulation of potential profile of the *p-i-n* junction as well as strain map and energy band diagram of a single QDs in a GaAs matrix, point to strong impact of Si doping of QDs on recombination losses via QD's states and, therefore, improvement of lifetime of the photoexcited electron-hole pairs due to appearance of the local electric fields in and around single QDs. We have shown earlier [22] that insertion of the InAs QD layers in the intrinsic layer of the QDSC leads to a decrease of the quantum efficiency from 11.0 % to 9.1 % and V_{oc} from 0.922 V to 0.777 V resulting from optical quality of the QD/bulk interface and lower contact potential difference of the *p-i-n* diode due to thermal escape of carriers from QDs to the *i*-GaAs. The similar problem has been widely observed for various type of QDSCs, and is one of the major issues for design of high-efficiency QDSCs [8,43]. Applying Si dopant to the QDs recover photovoltage as large as 105 mV and improve efficiency up to 9.5 % for 18e QDSC, although short-circuit gradually decreases from 17.2 mA/cm² for the 0e QDSC to

14.3 mA/cm² for the 24e QDSC. The studied SCs exhibit the filling factor in the range from 66 % to 70.4 %. Our findings indicate that recombination losses via QD states can be mitigated by local electric fields of Si dopants as well as strain-induced fields, which separate spatially the electron-hole pairs increasing their lifetime and prolonging the V_{OC} decay. Shrinking of the depletion layer resulted in appearance of flat band region with a modulation of the electrostatic potential in and around the QDs created by ionized Si impurities, which also facilitates improving of the SC's efficiency. At the same time, the important advantage of QDSC, viz., increased IR harvesting, is lost with Si doping due to filling of the QD ground states. Controlling the population of n -doped QDs as well as local barriers near QD/bulk interface is critical for producing highly efficient IBSCs.

IV. CONCLUSIONS

In this work, we have studied the effect of InAs QDs in the space-charge region of GaAs $p-i-n$ solar cells on recombination and photogeneration processes using photovoltage and photocurrent transient techniques. We have found that together with the enhanced photoresponse in the IR range, applying Si dopants to QDs significantly decreases the recombination losses via QDs, thereby, decreases dark current under reverse bias, and prolongs the photovoltage decay. The observed increase of photocurrent decay times with doping originates from an increase of the junction capacitance due to shrinking the depletion layer by the presence of ionized donors in the intrinsic layer. This is a clear signature of spatial redistribution of potential profiles inside the intrinsic layer by introduction of silicon doping directly in the QDs. The results of this work confirm that the negative built-in-dot charge has a considerable effect on harvesting of the infrared radiation below the band gap of GaAs and improvement of the lifetime of the photoexcited charge carriers due to appearance of the local electric fields in and around QDs.

AUTHOR INFORMATION

Corresponding Author

Serhiy V. Kondratenko

E-mail: kondr@univ.kiev.ua; Tel: +380674015816.

Yuriy I. Mazur

E-mail: ymazur@uark.edu.

Author Contributions

All authors contributed equally.

Notes

The authors declare no competing financial interest.

ACKNOWLEDGMENT

The authors acknowledge the support of the National Science Foundation of the U.S. (EPSCoR Grant # OIA-1457888).

REFERENCES

- [1] Shockley W., Queisser H. J. **1961**, J. Appl. Phys., 32, 510–519.
- [2] Luque A., Marti A. **1997**, Phys. Rev. Lett. 78, 5014–5017.
- [3] Hubbard S. M., Cress C. D., Bailey C. G., Raffaele R. P., Bailey S. G., Wilt D. M. **2008**, Appl. Phys. Lett. 92, 123512.

- [4] Sablon K. A., Little J. W., Mitin V., Sergeev A., Vagidov N., Reinhardt K. **2011**, Nano Lett. 11, 2311–2317.
- [5] Guimard D., Morihara R., Bordel D., Tanabe K., Wakayama Y., Nishioka M., Yasuhiko A. **2010**, Appl. Phys. Lett. 96, 203507.
- [6] Laghumavarapu R. B., El-Emawy M., Nuntawong N., Moscho A., Lester L. F., Huffaker D. L. **2007**, Appl. Phys. Lett. 91, 243115.
- [7] Ramiro I., Villa J., Lam P., Hatch S., Wu J., Lopez E., Antolin E., Liu H., Marti A., **2015**, IEEE J. Photovoltaics. 5, 840–845.
- [8] Tutu F. K., Wu J., Lam P., Tang M., Miyashita N., Okada Y., Wilson J., Allison R., Liu H. **2013**, Appl. Phys. Lett. 103, 043901.
- [9] Tutu F. K., Lam P., Wu J., Miyashita N., Okada Y., Lee K. H., Ekins-Daukes N. J., Wilson, J.; Liu, H. **2013**, Appl. Phys. Lett. 102, 163907.
- [10] Luque A., Marti A. **2010**, Adv. Mater. 22, 160–174.
- [11] Popescu V., Bester G., Hanna M. C., Norman A. G., Zunger A. **2008**, Phys. Rev. B - Condens. Matter Mater. 78, 205321.
- [12] Oshima R., Takata A., Okada Y. **2008**, Appl. Phys. Lett. 93, 083111.
- [13] Sablon K., Sergeev A., Vagidov N., Antipov A., Little J., Mitin V. **2011**, Nanoscale Res. Lett. 6, 584.
- [14] Luque A., Marti A., Lopez N., Antolin E., Canovas E., Stanley C., Farmer C., Diaz P. **2006**, J. Appl. Phys. 99, 094503.

- [15] Kunets V. P., Furrow C. S., Morgan T. Al., Hirono Y., Ware M. E., Dorogan V. G., Mazur Yu. I., Salamo G. J. **2012**, Appl. Phys. Lett. 101, 041106.
- [16] Shang X. J., He J. F., Li M. F., Zhan F., Ni H. Q., Niu Z. C., Pettersson H., Fu Y. **2011**, Appl. Phys. Lett. 99, 113514.
- [17] Asano T., Fang Z., Madhukar A. **2010**, J. Appl. Phys. 107, 073111.
- [18] Tutu F. K., Sellers I. R., Peinado M. G., Pastore C. E., Willis S. M., Watt A. R., Wang T., Liu H. Y. **2012**, J. Appl. Phys. 111, 046101.
- [19] Sablon K. A., Sergeev A., Vagidov N., Little J. W., Mitin V. **2012**, Sol. Energy Mater. Sol. Cells. 117, 638-644.
- [20] Zhou D., Vullum P. E., Sharma G., Thomassen S. F., Holmestad R., Reenaas T. W., Fimland B. O. **2010**, Appl. Phys. Lett. 96, 083108.
- [21] Okada Y., Morioka T., Yoshida K., Oshima R., Shoji Y., Inoue T., Kita T. **2011**, J. Appl. Phys. 109, 024301.
- [22] Lam P., Hatch S., Wu J., Tang M., Dorogan V. G., Mazur Y. I., Salamo G. J., Ramiroa, I., Seeds A., Liu H. **2014**, Nano Energy. 6, 159–166.
- [23] Di D., Perez-Wurfl I., Gentle A., Kim D., Hao X., Shi L., Conibeer G., Green M. A. **2010**, Nanoscale Res. Lett. 5, 1762–1767.
- [24] Luque A., Marti A., Stanley C. **2012**, Nat. Photonics. 6, 146–152.
- [25] Grundmann M. **2006**, The physics of semiconductors: An introduction including devices and nanophysics, 3rd ed, Springer International Pub., Switzerland.

- [26] Schmalz K., Yassievich I. N., Rucker H., Grimmeiss H. G., Frankenfeld H., Mehr W., Osten H. J., Schley P., Zeindl H. P. **1994**, Phys. Rev. B., 50, 14287–14301.
- [27] Anand S., Carlsson N., Pistol M. E., Samuelson L., Seifert W. **1998**, J. Appl. Phys. 84, 3747–3755.
- [28] Lang D. V. **1974**, J. Appl. Phys. 45, 3023–3032.
- [29] Blood P., Orton J. W. **1992**, The Electrical Characterization of Semiconductors: Majority Carriers and Electron States, Chapter 2, Academic Press: Michigan University.
- [30] Nextnano 3. “Device simulation package” [[http://www.nextnano.de/.](http://www.nextnano.de/)] (09 June **2011**).
- [31] Leonard D., Petroff P. M., Medeiros-Ribeiro G. **1995**, Appl. Phys. Lett. 66, 1767-1769.
- [32] Kondratenko S. V., Vakulenko O. V., Mazur Yu. I., Dorogan V. G., Marega Jr. E., Benamara M., Ware M. E., Salamo G. J. **2014**, J. Appl. Phys. 116, 193707.
- [33] Tasch A. F., Sah C. T. **1970**, Phys. Rev. B. 1, 800–809.
- [34] Wang K. L., Li G. P. **1983**, Solid State Commun. 47, 233–235.
- [35] Irmischer K., Klose H., Maass K. **1983**, Phys. Status Solidi. 25, 25–28.
- [36] Ganichev S., Ziemann E., Prettl W., Yassievich I., Istratov A., Weber E. **2000**, Phys. Rev. B. 61, 10361–10365.
- [37] Burstein E. **1954**, Phys. Rev. 93, 632-633.
- [38] Cappelluti F., Gioannini M., Khalili A. **2016**, Solar Energy Mat. and Solar Cells. 157, 209–220.

[39] Mitin V., Antipov A., Sergeev A., Vagidov N., Eason D., Strasser G. **2012**, *Nanoscale Res. Lett.* 7, 1–6.

[40] Höglund L., Holtz P. O., Pettersson H., Asplund C., Wang Q., Malm H., Almqvist S., Petrini E., Andersson J. Y. **2009**, *Appl. Phys. Lett.* 94, 053503.

[41] Casey H. C., Sell D. D., Wecht K. W. **1975**, *J. Appl. Phys.* 46, 250–257.

[42] Sze S. M., Lee M. K. **2012**, *Semiconductor Devices: Physics and Technology* 3rd ed, John Wiley & Sons Singapore Pte. Limited.

[43] Tayagaki T., Hoshi Y., Usami N. **2013**, *Sci. Rep.* 3, 2703.